Advanced Ceramics Progress: Vol. 12, No. 2, (Spring 2026) 79-92

Materials and Energy Research Center
MERC

Contents lists available at ACERP

Advanced Ceramics Progress

Journal Homepage: www.acerp.ir

Original Research Article

The Effect of Initial pH and Sonication Time on the Characteristics of ZnO Prepared in the Presence of Urea

Shahin Shoraka [a], Saeid Baghshahi [b,*], Mohammad Masoud Mohebi [c]

[a] *PhD Candidate, Department of Materials Science and Engineering, Faculty of Engineering, Imam Khomeini International University, Qazvin, Iran.*
[b] *Professor, Department of Materials Science and Engineering, Faculty of Engineering, Imam Khomeini International University, Qazvin, Iran.*
[c] *Associate Professor, Department of Materials Science and Engineering, Faculty of Engineering, Imam Khomeini International University, Qazvin, Iran.*

* Corresponding Author Email: baghshahi@eng.ikiu.ac.ir (S. Baghshahi)

URL: https://www.acerp.ir/article_258203.html

ARTICLE INFO

Article History:

Received 10 October 2026
Revised 02 November 2026
Accepted 25 November 2026

Keywords:

Zinc Oxide (ZnO),
Probe Sonochemistry,
Initial pH,
Sonication,
Synthesis

ABSTRACT

ZnO nanostructures were synthesized in the presence of urea by probe sonochemistry without post-synthetic calcination. The effects of sonication time and initial pH on the structural, morphological, optical, textural, and colloidal properties were examined at a fixed urea-to-zinc molar feed ratio. Sonication time ranged from 0 to 31 min at pH 10, whereas initial pH ranged from 8 to 12 at a fixed sonication time of 18 min. X-ray diffraction showed wurtzite ZnO as the dominant crystalline phase in all samples, while hydroxide- and carbonate-related secondary species depended on synthesis conditions. At pH 10, 18-min sonication provided optimal phase development. Increasing pH to 12 suppressed detectable secondary reflections, indicating the highest apparent phase purity. FE-SEM revealed an evolution from irregular agglomerates at pH 8 to well-defined hexagonal grains with central cavities at pH 10, and then to star-like tapered rods at pH 12. Surface chemistry, photoluminescence, texture, hydrodynamic size, and zeta potential varied with phase development and morphology. The A_{NBE}/A_{Defect} ratio decreased from 1.44 at pH 8 to 0.460 at pH 12, indicating increased defect-related emission at higher pH. The pH 12 sample exhibited the highest microstrain, whereas its near-neutral zeta potential indicated weak electrostatic stabilization despite its smaller hydrodynamic size. At pH 10, 18 min of sonication provided balanced phase development, well-defined hexagonal morphology, limited agglomeration, and electrostatic stability. In contrast, pH 12 favored apparent phase purity, stronger defect-related emission, and hierarchical morphology, but greater microstrain and reduced stabilization. The findings provide a process–structure–property basis for selecting conditions for specific applications.

https://doi.org/10.30501/acp.2026.606374.1212

1. INTRODUCTION

Zinc oxide (ZnO) is a multifunctional II–VI semiconductor with a wide direct band gap, high exciton binding energy, chemical stability, low cost, and versatile surface chemistry. These characteristics have supported its use in photocatalysis, sensing, optoelectronic devices, energy-conversion systems, and antimicrobial

Please cite this article as: Shoraka, S., Baghshahi, S., & Mohebi, M.M. (2026). The Effect of Initial pH and Sonication Time on the Characteristics of ZnO Prepared in the Presence of Urea. *Advanced Ceramics Progress*, *12*(2), 79-92. https://doi.org/10.30501/acp.2026.606374.1212

2423-7485/© 2026 The Author(s). Published by MERC.
This is an open access article under the CC BY license (https://creativecommons.org/licenses/by/4.0/).

technologies (Abou Zeid & Leprince-Wang, 2024; Chang et al., 2024; Clarke & Ghandi, 2023; Hasanah et al., 2024; Que et al., 2021; Uddin, 2026). ZnO is particularly relevant to environmental remediation because its surface properties, defect states, morphology, and charge-carrier behavior can influence adsorption, interfacial redox reactions, and photocatalytic degradation processes (Ong et al., 2018; Zhu & Wang, 2025).

The functional properties of ZnO depend not only on its nominal composition but also on crystallinity, crystallite size, lattice distortion, morphology, exposed facets, surface hydroxylation, defect-related states, and aggregation behavior. Together, these characteristics influence light absorption, charge-carrier recombination, surface accessibility, and dispersion in aqueous media (Chang et al., 2024; Clarke & Ghandi, 2023; Ong et al., 2018). ZnO can be prepared in a wide range of architectures, including zero-dimensional nanoparticles, one-dimensional nanorods and nanowires, two-dimensional plates and sheets, and three-dimensional flower-like and other hierarchical assemblies (Bao et al., 2020; Jimenez-Cadena et al., 2010; Ng et al., 2013; Ong et al., 2018; Panda et al., 2013; Wary et al., 2025; Zhang et al., 2014). Achieving reproducible control over these structural features requires careful management of precursor chemistry, solution conditions, and energy input during synthesis (Adamou et al., 2023; Chang et al., 2024; Clarke & Ghandi, 2023; Haque et al., 2020).

ZnO nanostructures have been produced by vapor-phase techniques, including physical and chemical vapor deposition, as well as by solution-based routes such as sol–gel processing, precipitation, hydrothermal and solvothermal synthesis, microwave-assisted synthesis, and microemulsion methods (Chitra et al., 2024; Gerbreders et al., 2020; Jimenez-Cadena et al., 2010; Luu et al., 2024; Ng et al., 2013; Ong et al., 2018; Rustembekkyzy et al., 2024; Wai & Li, 2022; Zhang et al., 2014). Among these approaches, solution-based methods are attractive because of their relative simplicity, scalability, and capacity to control particle size, morphology, and crystallinity through changes in precursor composition and reaction conditions (Chang et al., 2024; Clarke & Ghandi, 2023; Gerbreders et al., 2020; Lv et al., 2014; Uddin, 2026). However, the formation of well-developed ZnO nanostructures commonly requires prolonged reaction times, elevated temperatures, or post-synthetic calcination. Such treatments may alter crystallite growth, defect populations, surface chemistry, and particle aggregation, thereby complicating direct control over the final material properties (Clarke & Ghandi, 2023; Ghamarpoor et al., 2024; Uddin, 2026).

Sonochemistry offers an alternative route to intensify chemical processes in liquid media. Its effects arise primarily from acoustic cavitation, in which bubbles nucleate, grow, and collapse during alternating compression and rarefaction cycles. Bubble collapse generates localized high-energy conditions, shock waves, microjets, and microstreaming, which can influence precursor hydrolysis, nucleation, crystal growth, particle fragmentation, and aggregation. The outcome of sonochemical synthesis is governed by several coupled parameters, including ultrasonic frequency, applied power, duty cycle, temperature, reactor configuration, precursor concentration, and sonication time. Recent work on sonochemical ZnO synthesis has confirmed that irradiation time can affect powder homogeneity, crystal size, and aspect ratio (Adamou et al., 2023; Fioravanti et al., 2024; Hee Cho et al., 2022; Khataee, Karimi, et al., 2015; Khorsand Zak et al., 2013; Qi et al., 2022; Rodríguez-Flores et al., 2025; Tiong et al., 2025).

Initial pH is another key parameter governing ZnO formation in solution. By controlling hydroxide concentration and zinc-species speciation, pH affects hydrolysis, condensation, intermediate formation, nucleation rate, crystal-growth direction, and surface charge. Consequently, changes in initial pH can alter phase composition, crystallite development, lattice strain, morphology, and aggregation. In aqueous ZnO synthesis, the availability of hydroxide ions affects the formation of zinc hydroxide- and zincate-related growth species and may change the relative growth rates of crystallographic planes (Chang et al., 2024; Ghamarpoor et al., 2024; Khataee, Soltani, et al., 2015; Uddin, 2026).

The present study examines the effects of sonication time and initial pH on ZnO prepared in the presence of urea by probe sonochemistry without post-synthetic calcination. The central question is whether synthesis conditions that improve ZnO phase development and morphological definition also yield a favorable combination of photoluminescence, textural, and aqueous colloidal characteristics. The contribution of this work lies in identifying trade-offs among these responses through an integrated analysis of two synthesis series sharing a common reference condition, with a fixed precursor formulation. This approach provides a basis for selecting synthesis conditions according to the required combination of properties rather than identifying an optimum from a single characteristic.

A controlled two-series design was used to distinguish the effects of sonication time and initial pH. In the first series, sonication time was varied from 0 to 31 min at an initial pH of 10. In the second series, initial pH was varied from 8 to 12 at a fixed sonication time of 18 min. The urea-to-zinc molar feed ratio, zinc precursor concentration, ultrasonic frequency, instrument-set power, pulse sequence, and temperature range were kept constant. Urea was retained as a fixed component of the precursor formulation; its independent contribution to the resulting properties was not evaluated. The condition at an initial pH of 10 and a sonication time of 18 min served as the common reference point for both experimental

series, enabling direct comparison of the effects of sonication time and initial pH.

The resulting materials were characterized by X-ray diffraction, field-emission scanning electron microscopy, Fourier-transform infrared spectroscopy, photoluminescence spectroscopy, nitrogen adsorption–desorption analysis, dynamic light scattering, and zeta-potential measurements. The objective was not to identify a universally optimal synthesis condition but to determine how sonication time and initial pH produce competing changes in phase composition, structural order, morphology, defect-related emission, powder texture, hydrodynamic aggregation, and electrokinetic behavior. The findings provide a process–structure–property basis for selecting synthesis conditions for ZnO prepared in the presence of urea without post-synthetic calcination, with a view to subsequent application-oriented studies, including potential photocatalytic applications.

2. MATERIALS AND METHODS

2.1. Materials

Zinc acetate dihydrate, $Zn(CH_3COO)_2 \cdot 2H_2O$ (≥99.5%, Merck, Germany), was used as the zinc precursor. Urea, $CO(NH_2)_2$ (≥99.5%, Merck, Germany), was used as a component of the precursor formulation. Sodium hydroxide, NaOH (≥99%, Merck, Germany), was used to adjust the initial pH of the reaction mixture. Quadruple-distilled deionized water was used to prepare all aqueous solutions. Ethanol (≥96%, Mojallali, Iran) was used for washing the synthesized precipitates. All reagents were used as received without further purification.

2.2. Sonochemical Synthesis

ZnO nanostructures were synthesized in the presence of urea by a probe-type sonochemical method. An aqueous solution of zinc acetate dihydrate (0.100 M) was prepared under magnetic stirring, and urea (0.0055 M) was added as a component of the precursor formulation.

The urea-to-zinc molar feed ratio was fixed at 0.055, corresponding to an N/Zn atomic feed ratio of 0.110.

The precursor solution was stirred for 30 min at room temperature to ensure homogeneity. The initial pH of the reaction mixture was adjusted to 8, 10, or 12 by dropwise addition of 1 M NaOH under continuous magnetic stirring. The pH was monitored using a benchtop pH meter (RTC, model SL-901) equipped with a combined glass electrode.

Immediately after pH adjustment, the reaction mixture was sonicated using an APU500a ultrasonic processor (Adeeco) equipped with a 12 mm titanium probe. Sonication was performed in a 250 mL borosilicate-glass beaker (Pyrex) containing 100 mL of the reaction mixture. The ultrasonic processor was operated at a fixed frequency of 20 kHz and an instrument-set power of 175 W. Sonication was applied in pulsed mode using 2-s on and 3-s off intervals, corresponding to a 40% duty cycle. The temperature of the reaction mixture was maintained within 25–30 °C throughout sonication using the built-in thermoceramic temperature-control system.

Following sonication, the precipitates were separated by centrifugation at 6000 rpm for 10 min. The collected solids were washed twice with deionized water and once with ethanol. The washed products were dried in a vacuum oven at 70 °C, gently ground using an agate mortar, and stored in sealed containers before characterization. No calcination or post-synthetic thermal treatment other than the controlled vacuum-drying step was applied.

2.3. Sample Nomenclature

The samples were designated UZ-pHxx-tYY, where UZ indicates ZnO prepared in the presence of urea, xx denotes the initial pH, and YY denotes the sonication time in minutes.

The samples prepared at an initial pH of 10 with sonication times of 0, 5, 18, and 31 min were designated UZ-pH10-t00, UZ-pH10-t05, UZ-pH10-t18, and UZ-pH10-t31, respectively. The samples prepared at a fixed sonication time of 18 min and initial pH values of 8, 10, and 12 were designated UZ-pH08-t18, UZ-pH10-t18, and UZ-pH12-t18, respectively. UZ-pH10-t18 was common to both experimental series and served as the shared reference condition.

2.4. Characterization

Crystalline phases and structural characteristics were examined by X-ray diffraction (XRD) using an X'Pert Pro diffractometer (Philips, the Netherlands) with Cu Kα radiation (λ = 1.5406 Å). Measurements were performed at 40 kV and 30 mA over a 2θ range of 10–80°, with a step size of 0.05° and a counting time of 1 s per step at room temperature. The diffraction patterns were used for phase identification and estimation of lattice parameters, unit-cell volume, c/a ratio, apparent crystallite size, and microstrain. Lattice parameters were calculated from the relevant reflections of hexagonal wurtzite ZnO. Apparent crystallite size and microstrain were estimated by the Williamson–Hall method using at least eight diffraction reflections for each sample. Since instrumental broadening was not independently determined or subtracted from the measured peak widths, the Williamson–Hall-derived crystallite-size and microstrain values were treated as comparative, model-dependent estimates rather than absolute structural parameters.

Morphology and apparent particle-size distribution were examined using a MIRA4 field-emission scanning electron microscope (FE-SEM; TESCAN, Czech Republic) operated at an accelerating voltage of 20 kV

with a secondary-electron detector. Prior to imaging, the powder samples were coated with a thin gold layer to improve electrical conductivity and minimize charging effects.

Fourier-transform infrared (FTIR) spectra were recorded using a Tensor 27 spectrometer (Bruker Optics, Germany) over the range of 400–4000 cm^{-1}, with a spectral resolution of better than 1 cm^{-1}. Measurements were performed using the KBr-pellet method. Approximately 1 mg of powder was mixed with approximately 200 mg of dry KBr, ground in an agate mortar, and pressed into a pellet. A blank KBr background spectrum was recorded before each measurement to minimize contributions from atmospheric moisture, carbon dioxide, and the KBr matrix.

Room-temperature photoluminescence (PL) spectra were recorded using an F-2700 fluorescence spectrophotometer (Hitachi High-Tech, Japan) equipped with a 150 W xenon lamp. The samples were excited at 325 nm, and emission spectra were collected over the range of 350–500 nm. The near-band-edge emission area, A_{NBE}, was calculated by trapezoidal integration over 360–390 nm, whereas the defect-related emission area, A_{Defect}, was integrated over 400–500 nm. The ratio A_{NBE}/A_{Defect} was used as a comparative indicator of the relative contributions of the two analyzed emission regions. This ratio was not interpreted as a direct measure of the concentration of a specific defect species.

Specific surface area, total pore volume, and pore-size distribution were determined from nitrogen adsorption–desorption measurements at 77 K using a BELSORP Mini II analyzer (MicrotracBEL, Japan). Prior to analysis, the samples were degassed at 200 °C under the operating conditions of the instrument. Specific surface area was calculated using the Brunauer–Emmett–Teller (BET) method over a relative-pressure range of 0.05–0.30. Total pore volume and pore-size distribution were estimated using the Barrett–Joyner–Halenda (BJH) method applied to the desorption branch of the isotherm. These parameters were interpreted as powder textural properties and may include contributions from both intraparticle pores and interparticle voids within particle aggregates.

Hydrodynamic size distribution and zeta potential were measured at 25 °C using a Zetasizer instrument (Malvern Instruments, United Kingdom). A small amount of each powder was dispersed in distilled water and bath-sonicated for 10 min before measurement. Hydrodynamic size distributions were determined from fluctuations in scattered-light intensity, whereas zeta potential was calculated from electrophoretic mobility measurements. Because dynamic light scattering is sensitive to large scattering entities, the reported Z-average values were interpreted as hydrodynamic sizes of the measured scattering population, including possible aggregates, rather than as the dimensions of individual ZnO crystallites.

3. RESULTS AND DISCUSSION

3.1. Crystalline Structure and Phase Composition (XRD)

The effects of sonication time and initial pH on the crystalline structure and phase composition of the ZnO samples prepared in the presence of urea were investigated by X-ray diffraction (XRD). The XRD patterns of the sonication-time series and pH series are presented in Figure 1a and b, respectively. All samples exhibited the characteristic diffraction reflections of hexagonal wurtzite ZnO (space group $P6_3mc$). These reflections are consistent with the standard ZnO reference pattern (JCPDS No. 01-079-0205), confirming that wurtzite ZnO was the dominant crystalline phase under all synthesis conditions.

The contribution of secondary reflections varied with sonication time. The non-sonicated sample, UZ-pH10-t00, displayed the most pronounced additional reflections, which were tentatively associated with zinc hydroxide- and hydroxycarbonate-related precursor-derived species. Following 5 min of sonication, the intensity of these reflections decreased substantially, indicating more advanced precursor conversion. The lowest contribution from secondary reflections was observed for UZ-pH10-t18. In contrast, a slight reappearance of secondary reflections was observed after 31 min of sonication. These results indicate that, under the conditions investigated, 18 min represented an effective sonication time for phase development. Further irradiation did not improve the diffraction pattern and was instead associated with a modest increase in residual secondary species.

The pH series showed a clearer variation in phase development. UZ-pH08-t18, prepared at an initial pH of 8, exhibited the most pronounced secondary reflections, suggesting incomplete conversion of zinc-containing intermediates under the less alkaline condition. Increasing the initial pH to 10 markedly reduced these reflections. For UZ-pH12-t18, no secondary reflections were detected within the resolution of the XRD measurement, indicating the highest apparent phase purity among the investigated samples. This trend suggests that the higher hydroxide concentration at pH 12 promoted more complete conversion of precursor-derived species toward wurtzite ZnO. However, the absence of detectable secondary reflections should be interpreted as apparent phase purity within the detection limit of the XRD method rather than definitive evidence of complete chemical purity.

The principal ZnO reflections shifted slightly and non-monotonically with sonication time. The (100), (002), and (101) peaks initially moved to lower 2θ values and

then partially shifted back toward higher angles as sonication time increased. This behavior indicates a modest, non-monotonic change in the apparent lattice state with sonication time.

The calculated lattice parameters showed a corresponding trend. Relative to UZ-pH10-t00, both a and c increased after 5 min of sonication, then decreased at 18 min and changed only marginally upon further sonication to 31 min. Overall, the lattice expanded initially and then partially contracted, consistent with a modest, non-unidirectional modification of the ZnO lattice state with sonication time. The c/a ratio remained nearly constant (approximately 1.600), whereas the unit-cell volume increased from 46.83 $Å^3$ for UZ-pH10-t00 to 47.32 $Å^3$ for UZ-pH10-t05, before decreasing to approximately 47.0 $Å^3$ for the samples prepared at longer sonication times. The initial lattice expansion followed by partial contraction suggests a condition-dependent change in the local lattice environment rather than a continuous structural evolution with sonication time.

The pH series exhibited smaller but measurable changes in peak position and lattice parameters. The (100) reflection shifted slightly to higher 2θ with increasing pH, whereas the (002) and (101) reflections showed a more pronounced increase between the lowest and intermediate pH followed by a small decrease at the highest pH. Overall, these variations indicate a modest, non-monotonic change in the apparent lattice state across the pH series. The a parameter decreased slightly with increasing pH, while the c parameter decreased initially and then increased slightly at the highest pH. Unit-cell volume changed only marginally, from 47.10 $Å^3$ at pH 8 to 47.04 $Å^3$ at pH 12. Similarly, the c/a ratio remained close to 1.601. These results show that the wurtzite ZnO framework was retained across the pH series, while the calculated lattice parameters changed modestly with the initial pH.

The Williamson–Hall-derived apparent crystallite size increased from 32.70 nm for UZ-pH10-t00 to 33.65 nm for UZ-pH10-t05 and then to 40.90 nm for UZ-pH10-t18. A negligible further increase was observed at 31 min, with an apparent crystallite size of 41.14 nm. The corresponding microstrain values were 0.068%, 0.070%, 0.120%, and 0.120%, respectively. The nearly identical apparent crystallite size and microstrain values for UZ-pH10-t18 and UZ-pH10-t31 suggest that the structural effects of sonication had largely reached a plateau after 18 min. Therefore, the reappearance of weak secondary reflections after 31 min is more likely related to changes in residual precursor-derived species or surface-associated phases than to further crystallite growth.

The apparent crystallite size increased with increasing pH during synthesis, from 39.96 nm at pH 8 to 40.90 nm at pH 10 and 54.16 nm at pH 12. Microstrain increased simultaneously from 0.092% to 0.120% and then to 0.260%, respectively. Thus, the pH 12 condition promoted the largest apparent crystallite-size estimate and the highest microstrain among the samples. This result indicates that the more alkaline synthesis condition favored apparent crystallite development but was associated with a higher estimated microstrain. The coexistence of larger crystallites and higher microstrain is consistent with the structural heterogeneity and anisotropic morphology observed for this sample by FE-SEM.

Overall, sonication time and initial pH affected phase development through different, condition-dependent pathways. At pH 10, sonication promoted phase development up to 18 min, whereas extending the treatment to 31 min provided no further improvement in the apparent crystallite parameters and coincided with a slight reappearance of secondary reflections. Increasing the initial pH promoted apparent phase purity, with UZ-pH12-t18 exhibiting no detectable secondary reflections within the XRD detection limit. However, this higher apparent phase purity was accompanied by the highest Williamson–Hall microstrain.

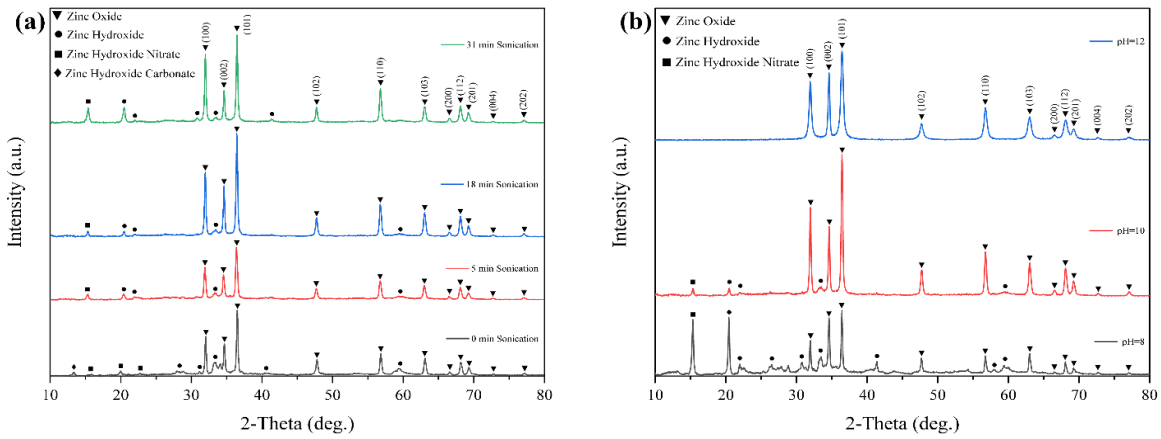

Figure 1. X-ray diffraction patterns of ZnO samples prepared in the presence of urea under different synthesis conditions: (a) sonication-time series at an initial pH of 10 and (b) initial-pH series at a fixed sonication time of 18 min

Therefore, UZ-pH10-t18 provided the most balanced structural condition within the sonication-time series, whereas UZ-pH12-t18 combined the highest apparent phase purity and the largest apparent crystallite-size estimate with the greatest lattice distortion.

3.2. Morphology and Microstructure (FE-SEM)

FE-SEM images of the ZnO samples prepared in the presence of urea are presented in Figure 2. Figure 2a compares the samples prepared at an initial pH of 10 with different sonication times, whereas Figure 2b shows the effect of initial pH at a fixed sonication time of 18 min. The FE-SEM images revealed particle morphology, apparent size uniformity, cavity formation, surface texture, and degree of agglomeration.

In the sonication-time series, the non-sonicated sample, UZ-pH10-t00, consisted predominantly of irregular and partially faceted agglomerates with a broad apparent size distribution. Although some hexagonal particles with central cavities were visible, they were strongly aggregated and their boundaries were not clearly resolved in many regions.

After 5 min of sonication, UZ-pH10-t05 showed more distinct hexagonal features, improved particle separation, and lower visible agglomeration relative to UZ-pH10-t00. The particle outlines were more clearly defined. These observations suggest that short-duration sonication was associated with improved particle separation and more clearly defined hexagonal features.

The most well-defined morphology within the sonication-time series was observed for UZ-pH10-t18. This sample was dominated by relatively uniform hexagonal plates with distinct edges, limited visible agglomeration, and central cavities in many particles, as seen in Figure 2(a). The central cavities may be associated with localized dissolution–reprecipitation during growth, in which the relatively defect-rich central region dissolves preferentially while ZnO deposition continues at the particle periphery. Acoustic cavitation may promote this process by enhancing micromixing and interfacial mass transfer. Taken together, these observations indicate that 18 min of sonication yielded the most well-defined particle morphology and the lowest visible agglomeration within the sonication-time series at an initial pH of 10.

Extending the sonication time to 31 min resulted in a less well-defined morphology. In UZ-pH10-t31, the hexagonal particle boundaries were less distinct, central cavities were not clearly visible in many particles, and denser agglomerates with rougher surfaces reappeared. This result suggests that prolonged sonication did not further improve particle refinement. Instead, it may have promoted particle reorganization and secondary aggregation during synthesis or subsequent drying.

A more pronounced morphological transition was observed in the pH series at a fixed sonication time of 18 min. UZ-pH08-t18, prepared at pH 8, consisted mainly of compact and irregular agglomerates in which individual particle boundaries were difficult to distinguish. The extensive agglomeration and poorly resolved particle boundaries indicate that an initial pH of 8 was less favorable for obtaining well-defined particle morphologies under the investigated synthesis conditions.

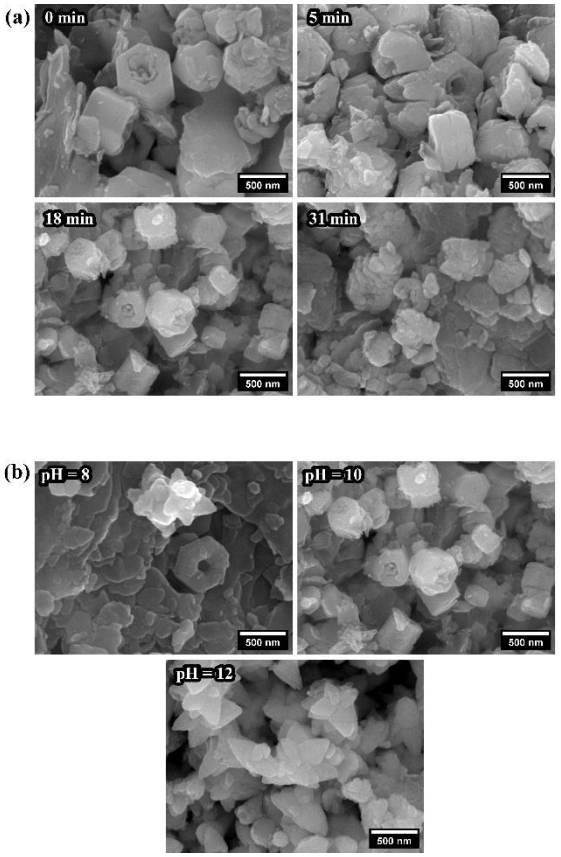

Figure 2. Representative FE-SEM images of ZnO samples prepared in the presence of urea under different synthesis conditions: (a) sonication-time series at an initial pH of 10, including UZ-pH10-t00, UZ-pH10-t05, UZ-pH10-t18, and UZ-pH10-t31; and (b) initial-pH series at a fixed sonication time of 18 min, including UZ-pH08-t18, UZ-pH10-t18, and UZ-pH12-t18

At pH 10, UZ-pH10-t18 showed relatively uniform, faceted hexagonal plates with limited visible agglomeration and distinct central cavities. Compared with the pH 8 sample, the particle boundaries were more clearly resolved.

At pH 12, UZ-pH12-t18 exhibited a markedly different morphology, consisting of star-like assemblies formed from tapered rod-like units radiating from common centers. Relative to UZ-pH10-t18, this sample showed a broader apparent size distribution, rougher surfaces, and a more open hierarchical architecture. The formation of these rod-based assemblies is consistent with a pH-dependent change in nucleation and growth behavior.

The higher hydroxide concentration likely altered the relative growth rates of different crystallographic directions, thereby favoring anisotropic growth and hierarchical assembly rather than compact hexagonal plate formation.

Overall, sonication time influenced particle separation and morphological definition at pH 10, whereas initial pH was associated with a transition from irregular agglomerates to hexagonal plates and star-like assemblies.

3.3. Surface Chemistry and Bonding (FTIR)

The spectra of the sonication-time and initial-pH series are shown in Figures 3(a) and 3(b), respectively.

In the sonication-time series, all samples exhibited a broad O–H stretching band attributed to surface hydroxyl groups or adsorbed water, together with a lower-wavenumber band assigned to Zn–O-related lattice vibrations. UZ-pH10-t00 additionally exhibited bands associated with Zn–OH-related vibrations and residual carbon-containing species, including carbonate- or carboxylate-related groups. Their presence is consistent with the greater contribution from precursor-derived secondary species indicated by XRD. However, FTIR alone cannot establish the exact crystalline identity of the hydroxide- or carbonate-containing phases responsible for these bands.

After 5 min of sonication, the Zn–OH-related feature was replaced by a band at a higher wavenumber, while C–O- and carboxylate-related bands remained detectable. At 18 min, the Zn–OH-related feature was no longer evident, the carbon-containing bands weakened substantially, and the Zn–O-related band shifted to a higher wavenumber relative to UZ-pH10-t00. These changes indicate a reduced contribution from precursor-derived hydroxide- and carbon-containing surface species, consistent with the improved phase development indicated by XRD and well-defined hexagonal morphology observed by FE-SEM. The Zn–O-related band shift is consistent with a change in the local bonding or lattice environment but does not directly establish a specific change in Zn–O bond strength.

At 31 min, the Zn–O-related band shifted slightly further to a higher wavenumber, a Zn–OH-related feature reappeared, and carbon-containing bands remained detectable. The O–H stretching band also shifted to a higher wavenumber relative to UZ-pH10-t18. These changes suggest an altered surface chemical environment and may indicate the persistence or reappearance of hydroxide- and carbon-containing species, consistent with the weak reappearance of secondary XRD reflections and renewed aggregation observed by FE-SEM.

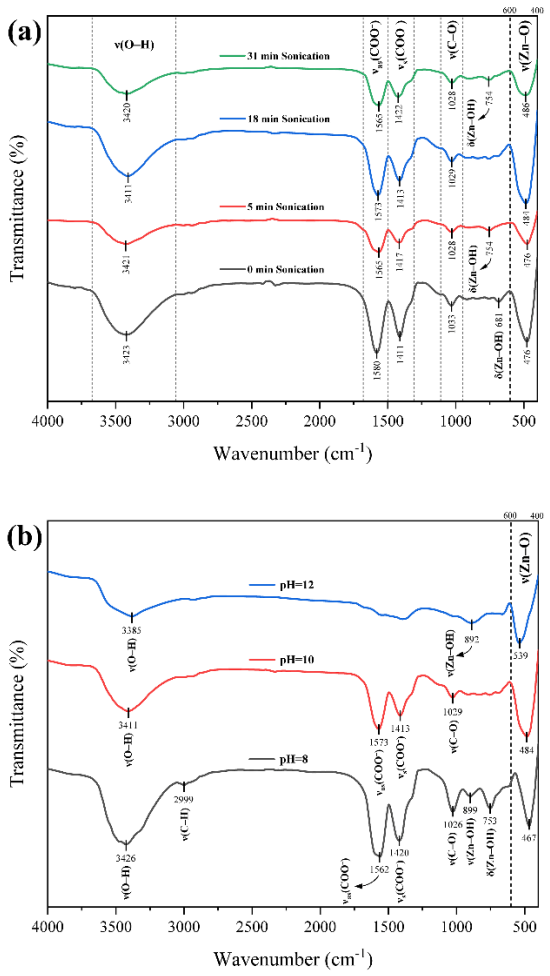

Figure 3. FTIR spectra of ZnO samples prepared in the presence of urea under different synthesis conditions: (a) sonication-time series at an initial pH of 10 and (b) initial-pH series at a fixed sonication time of 18 min. The principal Zn–O, O–H, Zn–OH, and carbon-containing vibrational regions are indicated

The initial-pH series exhibited more pronounced spectral changes. At pH 8, UZ-pH08-t18 showed Zn–OH-related features and residual carbon-containing bands, including those assigned to C–H-, C–O-, and carboxylate-related vibrations. Their relatively high intensity is consistent with the incomplete phase development indicated by XRD and extensive agglomeration observed by FE-SEM. At pH 10, the Zn–O-related band shifted to a higher wavenumber relative to the pH 8 sample, the Zn–OH-related features were absent, and the carbon-containing bands were absent or markedly weaker. This more ZnO-dominated spectral profile is consistent with the reduced contribution from secondary XRD reflections and the well-defined cavity-containing hexagonal plates observed by FE-SEM.

At pH 12, UZ-pH12-t18 exhibited a substantially higher-wavenumber Zn–O-related band and a Zn–OH-

related feature that reappeared, whereas C–O- and carboxylate-related bands were not detected. The broad O–H stretching band occurred at a lower wavenumber. These changes indicate a different local surface and lattice environment, consistent with the higher microstrain indicated by XRD and the star-like assemblies of tapered rod-like units observed by FE-SEM. Nevertheless, FTIR alone cannot establish the formation of a continuous hydroxide layer or identify the specific structural origin of the Zn–O-related band shift.

3.4. Defect-Related Optical Properties (PL)

The PL spectra of the sonication-time series and the initial-pH series are shown in Figures 4a and 4b, respectively.

In the sonication-time series, UZ-pH10-t00 showed A_{NBE} and A_{Defect} values of 953.6 and 750.6, respectively, resulting in an A_{NBE}/A_{Defect} ratio of 1.27. This was the highest ratio within the sonication-time series. However, both integrated emission areas were lower than those of the samples sonicated for 5 and 18 min. Therefore, the higher ratio for UZ-pH10-t00 should not be interpreted as evidence of superior optical quality or more efficient charge separation. Rather, it indicates a relatively larger NBE contribution within an overall weaker emission response.

After 5 min of sonication, A_{NBE} increased to 1105.0 and A_{Defect} increased to 944.2, giving a ratio of 1.17. Both integrated emission areas increased after 5 min of sonication, coinciding with the changes in phase development observed by XRD. At 18 min, the NBE and defect-related emission areas were 1022.0 and 1142.6, respectively, corresponding to an A_{NBE}/A_{Defect} ratio of 0.894. The decrease in this ratio indicates that defect-related emission became relatively more pronounced than NBE emission. Nevertheless, the substantial NBE contribution indicates that band-edge-related recombination remained significant. The PL response of UZ-pH10-t18 is consistent with the XRD, FE-SEM, and FTIR results, which collectively indicated favorable phase development, well-defined hexagonal morphology, and a reduced contribution from hydroxide-related surface species.

For UZ-pH10-t31, A_{NBE} decreased to 928.6, whereas A_{Defect} remained nearly unchanged at 1142.5. Consequently, the A_{NBE}/A_{Defect} ratio decreased further to 0.813. The lower ratio reflects a reduced relative contribution from the NBE interval within the analyzed spectrum; it does not, by itself, establish an improvement or deterioration in optical quality. This trend is consistent with the reappearance of Zn–OH-related FTIR features, the weak secondary reflections observed by XRD, and the denser aggregation observed by FE-SEM.

The effect of initial pH on the relative NBE and defect-related emission contributions was more pronounced. At pH 8, UZ-pH08-t18 showed A_{NBE} and A_{Defect} values of 869.8 and 603.5, respectively, resulting in an A_{NBE}/A_{Defect} ratio of 1.44. Although this was the highest ratio within the pH series, it should not be interpreted as evidence of a lower defect concentration or better optical quality. Both the defect-related emission area and the combined area of the analyzed NBE and defect-related emission regions were lower than those of the samples prepared at pH 10 and 12. The higher ratio therefore reflects a relatively greater contribution from the NBE region under conditions of incomplete phase development and poorly defined morphology.

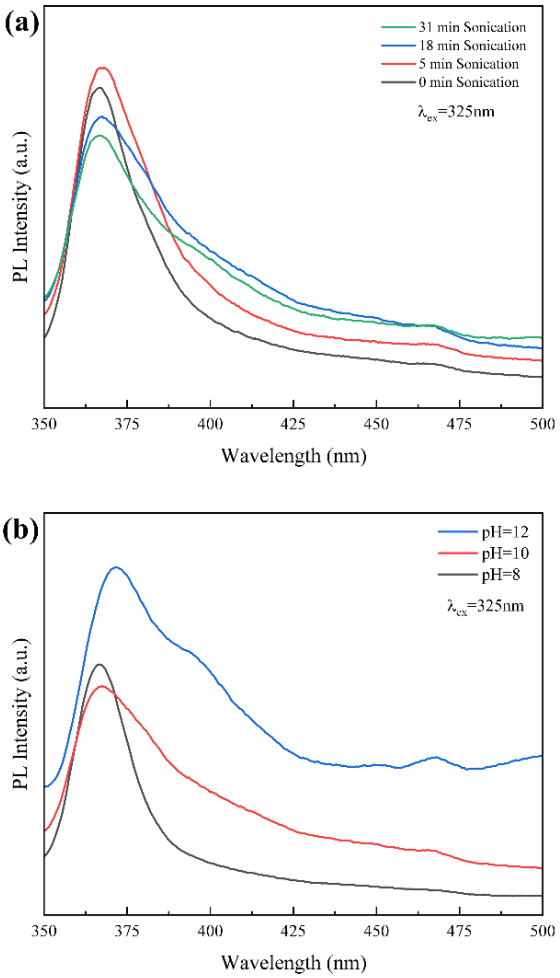

Figure 4. Room-temperature photoluminescence spectra of ZnO samples prepared in the presence of urea under different synthesis conditions: (a) sonication-time series at an initial pH of 10 and (b) initial-pH series at a fixed sonication time of 18 min

At pH 10, A_{NBE} and A_{Defect} increased to 1022.0 and 1142.6, respectively, giving an A_{NBE}/A_{Defect} ratio of 0.894. The increase in both emission regions coincided with the disappearance of Zn–OH-related FTIR bands, reduced secondary reflections in XRD, and the formation of well-defined cavity-containing hexagonal plates.

Compared with the pH 8 sample, the pH 10 sample exhibited a greater relative contribution from the 400–500 nm emission interval, together with fewer secondary XRD reflections and more clearly defined particle morphology.

A marked increase in emission intensity was observed for UZ-pH12-t18 at pH 12. The values of A_{NBE} and A_{Defect} were 1617.3 and 3520.0, respectively, resulting in an A_{NBE}/A_{Defect} ratio of 0.460. Thus, defect-related emission increased more strongly than NBE emission at pH 12. This behavior occurred together with the highest Williamson–Hall-derived microstrain, the marked shift in the Zn–O-related FTIR absorption region, and the morphological transition from cavity-containing hexagonal plates to star-like assemblies of tapered rod-like units.

The enhanced relative contribution of defect-related emission at pH 12 may be associated with the more strained lattice, greater surface complexity, and higher structural heterogeneity of this sample. However, the PL spectra do not allow the emission to be assigned to a single defect species. Visible emission in ZnO may arise from several bulk, surface, and adsorbate-related electronic states, and the present data are therefore interpreted broadly as defect-related and surface-associated emission.

Overall, both sonication time and initial pH altered the balance between NBE and defect-related emission, although the effects of initial pH were more pronounced. In the sonication-time series, 18 min of sonication produced a balanced PL response together with favorable phase development and morphology. Extending the treatment to 31 min further reduced the A_{NBE}/A_{Defect} ratio without providing evidence of structural improvement. In the pH series, increasing the initial pH from 8 to 12 reduced the A_{NBE}/A_{Defect} ratio from 1.44 to 0.460. This trend indicates an increasing relative contribution of defect-related emission as pH increased and is consistent with the concurrent changes in lattice strain, local bonding environment, and particle architecture.

3.5. Textural Properties (BET)

The textural properties of the ZnO powders prepared in the presence of urea were evaluated by nitrogen adsorption–desorption measurements at 77 K. The adsorption–desorption isotherms of the sonication-time series and the initial-pH series are presented in Figure 5a and b, respectively. The calculated BET specific surface area, total pore volume, BJH-derived average pore diameter, and hysteresis characteristics were interpreted together with the FE-SEM observations because the measured textural parameters may contain contributions from both intraparticle pores and interparticle voids within powder aggregates.

In the sonication-time series, the non-sonicated sample, UZ-pH10-t00, exhibited a type II isotherm with an H3 hysteresis loop. Its BET specific surface area was 18.33 $m^2 g^{-1}$, with a total pore volume of 0.0927 $cm^3 g^{-1}$ and a BJH-derived average pore diameter of 20.24 nm. The H3 hysteresis loop is commonly associated with slit-shaped voids formed between non-rigid aggregates or plate-like particle assemblies. Therefore, the relatively high surface area and pore volume of UZ-pH10-t00 should not be interpreted directly as evidence of a highly developed intrinsic porous structure. Instead, these values may reflect the irregular aggregation and interparticle voids observed in the FE-SEM images.

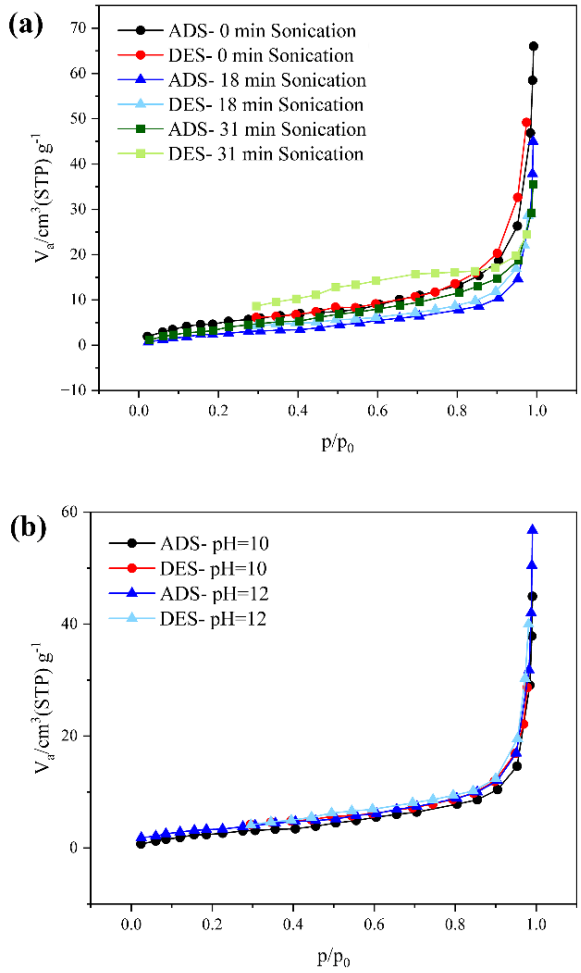

Figure 5. Nitrogen adsorption–desorption isotherms of ZnO samples prepared in the presence of urea under different synthesis conditions: (a) sonication-time series at an initial pH of 10 and (b) initial-pH series at a fixed sonication time of 18 min

After 18 min of sonication, UZ-pH10-t18 exhibited a type III isotherm with an H3 hysteresis loop. The BET specific surface area and total pore volume decreased to 9.82 $m^2 g^{-1}$ and 0.0638 $cm^3 g^{-1}$, respectively, whereas the BJH-derived average pore diameter increased to 25.97 nm. Compared with the non-sonicated sample, the lower

surface area and pore volume are consistent with the more well-defined hexagonal morphology and lower visible agglomeration observed by FE-SEM. The textural behavior of UZ-pH10-t18 may therefore be associated with a reduced contribution from irregular interparticle voids. However, the nitrogen adsorption–desorption data alone cannot distinguish unambiguously between changes in particle packing, accessible surface area, and the internal structure of individual particles.

For UZ-pH10-t31, prepared after 31 min of sonication, the isotherm remained type III with an H3 hysteresis loop. The specific surface area increased to 16.10 $m^2 g^{-1}$, while the total pore volume decreased further to 0.0539 $cm^3 g^{-1}$. The BJH-derived average pore diameter also decreased to 13.38 nm. The increase in BET surface area, together with the decrease in average pore diameter, is consistent with the formation of smaller and more closely packed voids within the powder structure. This observation agrees qualitatively with the FE-SEM images, which showed broader particle-size variation and renewed aggregation after prolonged sonication. Accordingly, the increase in apparent surface area at 31 min is more reasonably attributed to changes in particle assembly and interparticle contact than to the development of a uniformly porous ZnO framework.

The initial-pH series showed a clear difference between UZ-pH10-t18 and UZ-pH12-t18. UZ-pH10-t18, synthesized at pH 10, exhibited a specific surface area of 9.82 $m^2 g^{-1}$, a total pore volume of 0.0638 $cm^3 g^{-1}$, and an average pore diameter of 25.97 nm. At pH 12, UZ-pH12-t18 showed higher values of specific surface area and total pore volume, reaching 12.32 $m^2 g^{-1}$ and 0.0817 $cm^3 g^{-1}$, respectively, while the BJH-derived average pore diameter changed only slightly to 26.55 nm. The increase in surface area and pore volume at pH 12 is consistent with the more open, star-like morphology formed from tapered rod-like units. This hierarchical architecture may provide additional accessible external surfaces and interparticle voids relative to the compact hexagonal plates observed at pH 10.

Overall, the nitrogen adsorption–desorption data indicate that sonication time and initial pH influenced the apparent textural properties of the ZnO powders. Among the samples analyzed in the sonication-time series, UZ-pH10-t00 had the highest reported specific surface area and total pore volume. UZ-pH10-t18 had the lowest reported specific surface area, whereas UZ-pH10-t31 had the lowest total pore volume. Because UZ-pH10-t00 also showed extensive aggregation, its higher apparent surface area should not be considered inherently favorable without considering the morphology and particle assembly. Extending sonication to 31 min increased the specific surface area while decreasing both pore volume and average pore diameter, suggesting a more compact arrangement of smaller interparticle voids.

At a fixed sonication time of 18 min, increasing the initial pH from 10 to 12 increased both specific surface area and total pore volume. This trend corresponds with the transition from cavity-containing hexagonal plates to a more open hierarchical morphology. These observations suggest that particle morphology and aggregate structure contributed to the measured textural differences among the powders. Consequently, a higher BET surface area should not be interpreted independently as evidence of higher crystallinity, greater intrinsic porosity, improved surface accessibility in suspension, or superior colloidal stability.

3.6. Colloidal Behavior (DLS and Zeta Potential)

The colloidal behavior of the ZnO samples prepared in the presence of urea was evaluated in aqueous suspension by dynamic light scattering (DLS) and zeta-potential measurements. The DLS distributions of the sonication-time series and the initial-pH series are shown in Figure 6a and b, respectively. Because DLS is highly sensitive to large scattering entities, the reported Z-average values should be interpreted as hydrodynamic sizes of the measured scattering population, including particle aggregates, rather than as the dimensions of individual ZnO crystallites. This distinction is especially important for heterogeneous suspensions, in which a small number of large aggregates can strongly influence the intensity-weighted DLS signal.

In the sonication-time series, the non-sonicated sample, UZ-pH10-t00, showed a Z-average of 1742.1 nm and a PDI of 1.198. The mean size, mode size, and standard deviation obtained from the reported size distribution were 295.8, 294.5, and 36.8 nm, respectively. The high PDI indicates a highly heterogeneous suspension and limits the reliability of the cumulants-derived Z-average. The substantial difference between the Z-average and the distribution-derived mean and mode highlights the limitations of representing this sample by a single size value. This behavior is consistent with the extensive agglomeration observed in the FE-SEM images of the non-sonicated sample.

After 18 min of sonication, UZ-pH10-t18 exhibited a lower Z-average of 1088.1 nm and a PDI of 0.458. The corresponding mean size, mode size, and standard deviation were 296.0, 264.3, and 76.6 nm, respectively. The decrease in PDI relative to UZ-pH10-t00 indicates a lower degree of distribution heterogeneity under the applied measurement conditions. However, a PDI of 0.458 still indicates a polydisperse suspension, and the Z-average remains substantially larger than the apparent dimensions of the individual structures observed by FE-SEM. Therefore, sonication for 18 min improved the dispersion state relative to the non-sonicated condition but did not result in a suspension of individually dispersed primary particles.

Extending the sonication time to 31 min further decreased the Z-average to 838.7 nm, while the PDI increased to 0.597. The mean and mode sizes increased

to 334.9 and 298.4 nm, respectively, and the standard deviation increased to 88.4 nm. The lower Z-average was accompanied by a higher PDI, indicating that the decrease in the reported mean hydrodynamic size was not accompanied by a narrower cumulants-derived size distribution. This trend is consistent with the FE-SEM observations, which showed renewed aggregation and a broader apparent particle-size distribution after 31 min of sonication. Consequently, the lower Z-average of UZ-pH10-t31 should not be interpreted independently as evidence of improved colloidal stability.

The zeta potential varied non-monotonically with sonication time. UZ-pH10-t00, UZ-pH10-t18, and UZ-pH10-t31 exhibited zeta-potential values of +51.3, +41.5, and +61.4 mV, respectively. The corresponding electrophoretic mobilities were +0.000396, +0.000321, and +0.000475 $cm^2\ V^{-1}\ s^{-1}$, respectively. All three samples had zeta-potential magnitudes greater than 30 mV, a commonly used empirical threshold for assessing electrostatic stabilization. Nevertheless, zeta potential should not be interpreted as a direct measure of aggregate size or long-term dispersion behavior. It depends on the particle–liquid interface and may be affected by surface chemistry, suspension pH, ionic strength, particle shape, and the electrokinetic model used to convert electrophoretic mobility to zeta potential. The non-monotonic variation observed here is consistent with the sonication-dependent changes in surface-related FTIR features, but it cannot be attributed to a single functional group or defect population.

The effect of initial pH was more pronounced in the comparison between UZ-pH10-t18 and UZ-pH12-t18. The sample synthesized at an initial pH of 10, UZ-pH10-t18, showed a Z-average of 1088.1 nm, a PDI of 0.458, a mean size of 296.0 nm, a mode size of 264.3 nm, and a standard deviation of 76.6 nm. Its zeta potential was +41.5 mV, with an electrophoretic mobility of +0.000321 $cm^2\ V^{-1}\ s^{-1}$. For the powder synthesized at an initial pH of 10, the positive zeta potential of +41.5 mV indicates substantial electrostatic repulsion between suspended particles under the measurement conditions.

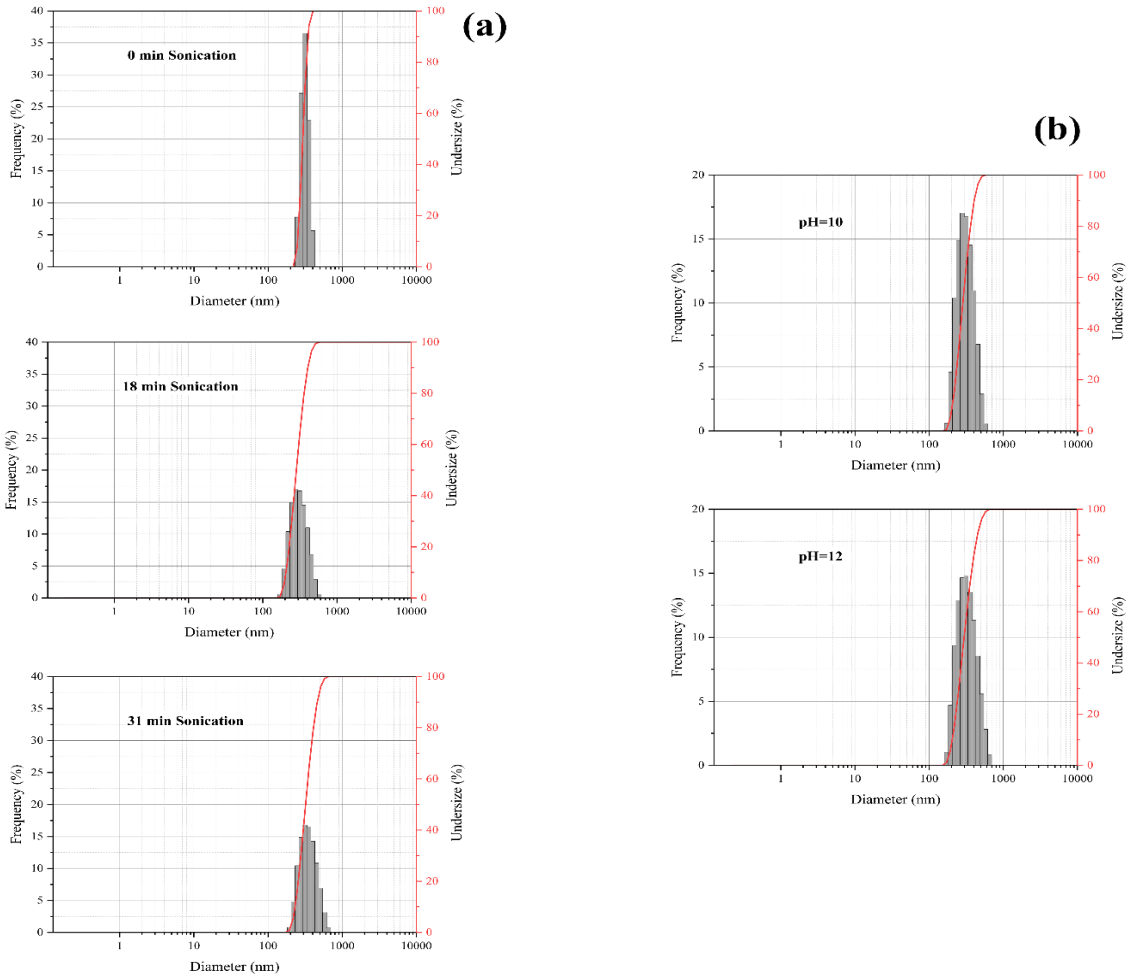

Figure 6. Dynamic light-scattering size distributions of aqueous suspensions of ZnO prepared in the presence of urea under different synthesis conditions: (a) sonication-time series at an initial pH of 10 and (b) initial-pH series at a fixed sonication time of 18 min. Zeta-potential values are discussed in the text

The sample synthesized at an initial pH of 12, UZ-pH12-t18, exhibited a lower Z-average of 501.1 nm and a lower PDI of 0.382. The mean size, mode size, and standard deviation were 313.8, 295.2, and 94.5 nm, respectively. Although the measured Z-average and PDI were lower than those of UZ-pH10-t18, the zeta potential decreased sharply to −2.1 mV, with an electrophoretic mobility of −0.000016 $cm^2 V^{-1} s^{-1}$. This near-neutral zeta potential indicates weak electrostatic stabilization under the applied measurement conditions. Therefore, the lower Z-average of UZ-pH12-t18 should not be interpreted as proof of better long-term colloidal stability.

For UZ-pH12-t18, the smaller measured Z-average and near-neutral zeta potential describe different aspects of the suspension and are not inherently contradictory. The former characterizes the measured hydrodynamic response, whereas the latter suggests a limited contribution from electrostatic repulsion under the measurement conditions. These observations do not establish long-term dispersion stability or complete deagglomeration into primary particles.

Overall, the measured hydrodynamic and electrokinetic properties varied with sonication time and initial synthesis pH. At pH 10, sonication reduced the extreme distribution heterogeneity of the non-sonicated suspension, as indicated by the reduction in PDI from 1.198 for UZ-pH10-t00 to 0.458 for UZ-pH10-t18. Extending the sonication time to 31 min further decreased the measured Z-average but increased the PDI, indicating a broader and more heterogeneous distribution. In the pH series, increasing the initial pH from 10 to 12 decreased the measured Z-average and PDI but shifted the zeta potential from +41.5 to −2.1 mV, indicating a substantial loss of electrostatic stabilization. Among the samples for which colloidal data were reported, UZ-pH10-t18 showed the most balanced combination of reduced distribution heterogeneity and a strongly positive zeta potential. In contrast, UZ-pH12-t18 exhibited the smallest measured hydrodynamic size but weak electrostatic protection against aggregation.

4. CONCLUSIONS

ZnO prepared in the presence of urea by probe sonochemistry without post-synthetic calcination exhibited synthesis-dependent properties, with wurtzite ZnO remaining the dominant crystalline phase across all investigated conditions. At an initial pH of 10, 18 min of sonication improved phase development and morphological definition, whereas extending sonication to 31 min produced little change in the apparent crystallite size and estimated microstrain and coincided with renewed agglomeration and weak secondary XRD reflections.

Increasing initial pH from 8 to 12 transformed irregular agglomerates into cavity-containing hexagonal plates and subsequently star-like rod assemblies. The sample synthesized at an initial pH of 12 showed no detectable secondary XRD reflections and had the highest estimated microstrain. Across the pH series, the A_{NBE}/A_{Defect} ratio decreased from 1.44 to 0.460, indicating a greater relative contribution from the analyzed 400–500 nm emission interval without identifying specific defect species or their concentrations.

Textural and colloidal measurements revealed trade-offs. Among the samples analyzed in the sonication-time series, the non-sonicated sample had the highest reported specific surface area and total pore volume, which may include contributions from interparticle voids. Of the samples analyzed in the pH series, the powder synthesized at an initial pH of 12 had the lowest measured Z-average and PDI, but its near-neutral zeta potential (−2.1 mV) indicated weak electrostatic stabilization under the measurement conditions.

Overall, an initial pH of 10 and a sonication time of 18 min provided a balanced combination of the investigated characteristics, including well-defined hexagonal morphology and a zeta potential of +41.5 mV under the measurement conditions. These characteristics provide a basis for selecting synthesis conditions for potential photocatalytic and other application-oriented studies; direct evaluation of functional performance is required in future work.

ACKNOWLEDGEMENTS

The authors gratefully acknowledge Imam Khomeini International University (IKIU) for providing the laboratory facilities and equipment used in this work.

REFERENCES

1. Abou Zeid, S., & Leprince-Wang, Y. (2024). Advancements in ZnO-Based Photocatalysts for Water Treatment: A Comprehensive Review. In *Crystals*, Vol. 14, Number 7, 611. https://doi.org/10.3390/cryst14070611

2. Adamou, P., Harkou, E., Hafeez, S., Manos, G., Villa, A., Al-Salem, S. M., Constantinou, A., & Dimitratos, N. (2023). Recent progress on sonochemical production for the synthesis of efficient photocatalysts and the impact of reactor design. *Ultrasonics Sonochemistry*, Vol. 100, 106610. https://doi.org/10.1016/j.ultsonch.2023.106610

3. Bao, Y., Gao, L., Feng, C., Ma, J., Zhang, W., Liu, C., & Simion, D. (2020). Sonochemical synthesis of flower-like ZnO assembled by hollow cones toward water vapor permeability and water resistance enhancement of waterborne film. *Journal of Industrial and Engineering Chemistry, 82*, 180–189. https://doi.org/10.1016/j.jiec.2019.10.011

4. Chang, J. Sen, Saint, C. P., Chow, C. W. K., Bahnemann, D. W., & Chong, M. N. (2024). Recent innovations in engineering Zinc Oxide (ZnO) nanostructures for water and wastewater treatment: Pushing the boundaries of multifunctional photocatalytic and advanced biotechnological applications. In *International Materials Reviews*, Vol. 69, Numbers 7–8, 337–379. https://doi.org/10.1177/09506608241280421

5. Chitra, M., Kistan, A., Kanchana, V., & Jayanthi, A. (2024). Sol-Gel synthesis, characterization and photocatalytic activity of Cobalt doped ZnO nanoparticles. *Research Journal of Chemistry and Environment, 28*(3), 48–55. https://doi.org/10.25303/283rjce048055

6. Clarke, B., & Ghandi, K. (2023). The Interplay of Growth Mechanism and Properties of ZnO Nanostructures for Different Applications. In *Small*, Vol. 19, Number 44, 2302864. https://doi.org/10.1002/smll.202302864

7. Fioravanti, A., Mazzocchi, M., Marani, P., Pedrielli, F., Carotta, M. C., Sacerdoti, M., Valsania, M. C., & Morandi, S. (2024). Highly Efficient and Reproducible Sonochemical Synthesis of ZnO Nanocrystals. *ChemPlusChem, 89*(7), e202400005. https://doi.org/10.1002/cplu.202400005

8. Gerbreders, V., Krasovska, M., Sledevskis, E., Gerbreders, A., Mihailova, I., Tamanis, E., & Ogurcovs, A. (2020). Hydrothermal synthesis of ZnO nanostructures with controllable morphology change. *CrystEngComm, 22*(8), 1346–1358. https://doi.org/10.1039/c9ce01556f

9. Ghamarpoor, R., Fallah, A., & Jamshidi, M. (2024). A Review of Synthesis Methods, Modifications, and Mechanisms of ZnO/TiO2-Based Photocatalysts for Photodegradation of Contaminants. In *ACS Omega*, Vol. 9, Number 24, 25457–25492. https://doi.org/10.1021/acsomega.3c08717

10. Haque, M. J., Bellah, M. M., Hassan, M. R., & Rahman, S. (2020). Synthesis of ZnO nanoparticles by two different methods & comparison of their structural, antibacterial, photocatalytic and optical properties. *Nano Express, 1*(1), 010007. https://doi.org/10.1088/2632-959X/ab7a43

11. Hasanah, A. U., Ikbal, M. S., & Tahir, D. (2024). Advances in Rare Earth-Doped ZnO Photocatalysts: Enhancing Photogenerated Electron-Hole Pairs for Radical Atom Generation. In *ChemBioEng Reviews*, Vol. 11, Number 3, 595–612. https://doi.org/10.1002/cben.202300058

12. Hee Cho, C., Choe, Y. S., Chae, S., & Il Lee, T. (2022). Highly sensitive breath sensor based on sonochemically synthesized cobalt-doped zinc oxide spherical beads. *Ultrasonics Sonochemistry, 84*, 105956. https://doi.org/10.1016/j.ultsonch.2022.105956

13. Jimenez-Cadena, G., Comini, E., Ferroni, M., Vomiero, A., & Sberveglieri, G. (2010). Synthesis of different ZnO nanostructures by modified PVD process and potential use for dye-sensitized solar cells. *Materials Chemistry and Physics, 124*(1), 694–698. https://doi.org/10.1016/j.matchemphys.2010.07.035

14. Khataee, A., Karimi, A., Arefi-Oskoui, S., Darvishi Cheshmeh Soltani, R., Hanifehpour, Y., Soltani, B., & Joo, S. W. (2015). Sonochemical synthesis of Pr-doped ZnO nanoparticles for sonocatalytic degradation of Acid Red 17. *Ultrasonics Sonochemistry, 22*, 371–381. https://doi.org/10.1016/j.ultsonch.2014.05.023

15. Khataee, A., Soltani, R. D. C., Karimi, A., & Joo, S. W. (2015). Sonocatalytic degradation of a textile dye over Gd-doped ZnO nanoparticles synthesized through sonochemical process. *Ultrasonics Sonochemistry, 23*, 219–230. https://doi.org/10.1016/j.ultsonch.2014.08.023

16. Khorsand Zak, A., Majid, W. H. A., Wang, H. Z., Yousefi, R., Moradi Golsheikh, A., & Ren, Z. F. (2013). Sonochemical synthesis of hierarchical ZnO nanostructures. *Ultrasonics Sonochemistry, 20*(1), 395–400. https://doi.org/10.1016/j.ultsonch.2012.07.001

17. Luu, T. V. H., Nguyen, H. Y. X., Nguyen, Q. T., Nguyen, Q. B., Nguyen, T. H. C., Pham, N. C., Nguyen, X. D., Nguyen, T. K., & Dao, N. N. (2024). Enhanced photocatalytic performance of ZnO under visible light by co-doping of Ta and C using hydrothermal method. *RSC Advances*, 14(18), 12954–12965. https://doi.org/10.1039/d4ra00579a

18. Lv, J., Shang, F., Pan, G., Wang, F., Zhou, Z., Liu, C., Gong, W., Zi, Z., Chen, X., He, G., Zhang, M., Song, X., Sun, Z., & Liu, F. (2014). Effect of solution concentration on surface morphology and photocatalytic activity of ZnO thin films synthesized by hydrothermal methods. *Journal of Materials Science: Materials in Electronics, 25*(2), 882–887. https://doi.org/10.1007/s10854-013-1660-x

19. Ng, S. M., Wong, D. S. N., Phung, J. H. C., & Chua, H. S. (2013). Integrated miniature fluorescent probe to leverage the sensing potential of ZnO quantum dots for the detection of copper (II) ions. *Talanta, 116*, 514–519. https://doi.org/10.1016/j.talanta.2013.07.031

20. Ong, C. B., Ng, L. Y., & Mohammad, A. W. (2018). A review of ZnO nanoparticles as solar photocatalysts: Synthesis, mechanisms and applications. *Renewable and Sustainable Energy Reviews, 81*, 536–551. https://doi.org/10.1016/j.rser.2017.08.020

21. Panda, N. R., Acharya, B. S., & Nayak, P. (2013). Sonochemical synthesis of nitrogen doped ZnO nanorods: Effect of anions on growth and optical properties. *Journal of Materials Science: Materials in Electronics, 24*(10), 4043–4049. https://doi.org/10.1007/s10854-013-1359-z

22. Qi, K., Zhuang, C., Zhang, M., Gholami, P., & Khataee, A. (2022). Sonochemical synthesis of photocatalysts and their applications. *Journal of Materials Science and Technology, 123*, 243–256. https://doi.org/10.1016/j.jmst.2022.02.019

23. Que, M., Lin, C., Sun, J., Chen, L., Sun, X., & Sun, Y. (2021). Progress in zno nanosensors. In *Sensors*, Vol. 21, Number 16, 5502. https://doi.org/10.3390/s21165502

24. Rodríguez-Flores, T., Hernández-Pérez, I., de la Huerta-Hernández, G. E., Ayala-Parada, Y., Cadena-Silva, J. G., & Haro-Pérez, C. (2025). Comparison of Photocatalytic Performance of Sonochemically Synthesized ZnO with Different Capping Agents. *ACS Omega*, 10 (28), 30181–30193. https://doi.org/10.1021/acsomega.5c00929

25. Rustembekkyzy, K., Sabyr, M., Kanafin, Y. N., Khamkhash, L., & Atabaev, T. S. (2024). Microwave-assisted synthesis of ZnO structures for effective degradation of methylene blue dye under solar light illumination. *RSC Advances, 14*(23), 16293–16299. https://doi.org/10.1039/d4ra02451f

26. Tiong, T. J., Chu, J. K., & Tan, K. W. (2025). Advancements in Acoustic Cavitation Modelling: Progress, Challenges, and Future Directions in Sonochemical Reactor Design. *Ultrasonics Sonochemistry, 112*. https://doi.org/10.1016/j.ultsonch.2024.107163

27. Uddin, I. (2026). Advances in Zinc Oxide Nanoparticles: Synthesis, Characterization, Applications, and Future Prospects. *Advanced Nano Research, 9*(1), 1–16. https://doi.org/10.21467/anr.9.1.1-16

28. Wai, H. S., & Li, C. (2022). Effect of Aluminum Doping Ratios on the Properties of Aluminum-Doped Zinc Oxide Films

Deposited by Mist Chemical Vapor Deposition Method Applying for Photocatalysis. *Nanomaterials, 12*(2). https://doi.org/10.3390/nano12020195

29. Wary, R. R., Das, A., Amirov, E. S., Liu, D., Gumber, S., Kazakova, E. A., Vasenko, A. S., & Prezhdo, O. V. (2025). Highly Oriented Nitrogen-Doped Flower-like ZnO Nanostructures for Boosting Photocatalytic and Photoelectrochemical Performance: A Combined Experimental and DFT Study. *Journal of Physical Chemistry Letters, 16*(20), 5180–5187. https://doi.org/10.1021/acs.jpclett.5c01085

30. Zhang, X., Qin, J., Xue, Y., Yu, P., Zhang, B., Wang, L., & Liu, R. (2014). Effect of aspect ratio and surface defects on the photocatalytic activity of ZnO nanorods. *Scientific Reports, 4*. https://doi.org/10.1038/srep04596

31. Zhu, C., & Wang, X. (2025). Nanomaterial ZnO Synthesis and Its Photocatalytic Applications: A Review. In *Nanomaterials*, Vol. 15, Number 9. https://doi.org/10.3390/nano15090682